https://doi.org/10.5194/egusphere-2026-1706
Preprint. Discussion started: 4 May 2026


# Measurement Report: Aircraft-Ground Observation Study of a Spring Snowstorm Event in the North China Plain: Cloud Microphysical Characteristics and Precipitation Vertical Structure

Can Song[1,2], Chong Peng[1,2], Ting Bai[1,2], Honglei Wang[3], Yimei Huang[1,2], Jianfang Ding[1,2], Yanhua Liu[1,2], Zhenping Shao[1,2], Xiuzhu Sha[1,2]

[1]Henan Key Laboratory of Agrometeorological Support and Applied Technique, CMA, Zhengzhou, 450003, China

[2]Weather Modification Center of Henan Province, Zhengzhou, 450003, China

[3]China Meteorological Administration Aerosol-Cloud and Precipitation Key Laboratory, Nanjing University of Information Science and Technology, Nanjing 210044, China

*Correspondence to*: Chong Peng (rushpeng@163.com)

**Abstract.** Studies on the characteristics of snowfall cloud systems contribute to understanding the mechanisms of snow formation and development. In this study, based on observations from King Air 350 and ground–based radar, the microphysical characteristics and vertical structure of precipitation during a spring snowstorm with thunderstorm on March 16, 2023 in the North China Plain are investigated. High concentrations of ice crystals (up to 131.1 $L^{-1}$) and limited small-scale cloud droplets (less than 10 $cm^{-3}$) was observed in the stratiform cloud area. In regions with heavy snowfall and elevated thunderstorm, the liquid water content in the upper cloud layer (~-18°C) is significantly higher than in other areas. Precipitations in these regions exhibited a vertical structure of aggregates and vertical ice crystals above, supercooled water in the middle, and graupel below. During the mid-phase of precipitation in Shangqiu, snow particles partially melted within the warm layer (1.8–2.4 km), increasing the equivalent reflectance factor ($Z_e$) and doppler velocity ($V$). And then it refreeze in the sub-zero temperature zone and finally completely melt into liquid droplets below 0.7 km. In the early and late stages, snow melting into wet snowflakes below 0.5 km significantly enhanced the $Z_e$, $V$ and spectrum width ($W$). During the late stage, updrafts promoted ice crystal growth and accumulation at 1.5–2.3 km, leading to a peak in $Z_e$ and positive value of $V$. The vertical structure and phase evolution of precipitation revealed here are significant for understanding the microphysical processes during hydrometeors falling, providing insights to improve precipitation type prediction accuracy.

https://doi.org/10.5194/egusphere-2026-1706
Preprint. Discussion started: 4 May 2026


## 1 Introduction

Heavy snowfall is a high–impact weather event in China, posing a serious threats to agricultural production and transportation. For solid precipitation, quantitative measurements of precipitation intensity are challenging. It is difficult to obtain the relationship between radar reflectivity factor and actual precipitation intensity (the $Z$–$R$ relationship), since the precipitation particles of different phases and shapes exhibit substantial differences in physical characteristics such as dielectric constant, density and terminal velocity (Szyrmer and Zawadzki, 2010; Tao et al., 2021; Barthazy and Schefold, 2006; Mai et al., 2023).

Studies on the microphysical characteristics of snowfall cloud systems contribute to understanding the mechanisms of snow formation and development. Precipitation particles undergo a series of complex microphysical processes, including collision and break–up (Hu and Srivastava, 1995; Low and List, 1982), from their formation until they reach the ground. Their physical characteristics such as phase and drop size distribution change significantly during the journey of falling (Wen et al., 2017; Wang et al., 2017; Wen et al., 2016; Das et al., 2010; Tokay et al., 2009). These changes are influenced by atmospheric thermal stratification and cloud microphysical properties (Rosenfeld and Ulbrich, 2003), making the forecasting of both surface precipitation intensity and phase particularly challenging. Therefore, observational research on the vertical structure and microphysical characteristics of snowfall is highly necessary.

The application of dual polarization radar and millimeter wave cloud radar has significantly enhanced the capability to detect the phase, size, and other microphysical parameters like ice water content(Zhao et al., 2025; Liao et al., 2016). Through polarization parameters such as the differential reflectivity factor, the phase of precipitation particles were effectively identified (Bechini and Chandrasekar, 2015; Dolan et al., 2013; Trefalt et al., 2018) and the growth mechanisms of ice crystals was quantified (Li et al., 2018), supporting short–term nowcasting for snowfall. MRR provides an observational means for studying the vertical structure of different precipitation types (Andrews et al., 2025; Wen et al., 2024; Das et al., 2017). Based on new methods for identification of bright band (Cha et al., 2009) and distinguishing precipitation phase(Maahn and Kollias, 2012; Makino et al., 2019; Garcia-Benadi et al., 2020), solid–-phase precipitation is researched recently (He et al., 2021; Zhou et al., 2024).

Aircraft-based observation is the most direct method for measuring cloud microphysical characteristics and provide valuable validation data for radar retrievals(Finlon et al., 2016). Some scholars have conducted studies on the vertical distribution of ice habits via visual inspection based on optical particle images(Feng et al., 2021b; Wang et al., 2023b). Particle habits classification methods based on particle shape parameters (Holroyd, 1987) or machine learning techniques(Tao et al., 2021; Xiao et al., 2019), are developed. Wang et al. (2023b) analyzed the shape characteristics of cloud particles across different temperatures and cloud systems using the classification method. Snow crystal spectrum distribution and is very important for the prediction of precipitation and radiation processes. Ice crystal and snow spectra at different altitudes and temperatures in different regions were investigated to analyze the mechanisms of snowfall(Woods et al., 2008; Feng et al., 2021a). Geerts et al. (2015) conducted aircraft observations of 16 mixed–phase shallow cloud snowfall events in Wyoming, analyzed the growth, transport, and deposition mechanisms of snowfall under different dynamic processes.

The North China Plain serves as a vital grain production base and a demographic and economic core region of China. Therefore, in–depth research on the formation mechanisms and patterns of

https://doi.org/10.5194/egusphere-2026-1706
Preprint. Discussion started: 4 May 2026


extreme weather events affecting this area, such as snowstorms, holds crucial practical significance for disaster prevention, and ensuring agricultural production. Wu et al. (2021) found that snowband contained three distinct layers: a condensational growth layer formed by ice crystals seeded from upper levels, an aggregation layer, and a riming layer by analyzing the vertical structure of snowfall in the Beijing region base on Ka and X–band dual–polarization radars. Wang et al. (2023a) identified the particle phase in a typical stratiform cloud case in Shandong and analyzed the rain–snow transition process. Huang et al. (2021) studied a stable snowfall event in Beijing. It shows that the liquid water content in the cloud was extremely low, and ice crystals grew primarily through deposition and aggregation processes, with minimal riming observed and no secondary ice formation detected. Abundant supercooled water was found within the warm and moist conveyor belt during a snowfall event in Hebei, where ice crystals from upper levels undergo riming growth as they pass through this layer, producing a large number of columnar ice crystals via the Hallett–Mossop multiplication mechanism (Wang et al., 2023b).

Airborne microphysical measurements of snowfall cloud systems in the North China Plain have primarily focused on stable cloud systems with radar echoes below 25 dBZ (Huang et al., 2021; Wang et al., 2023b; Mai et al., 2023). And the research on heavy snowfall events in North China has primarily focused on synoptic circulation patterns and radar observation analysis (Peng et al., 2015; Pei et al., 2012; Li et al., 2017). However, research on the vertical precipitation structure and microphysical characteristics about spring snowstorms based on aircraft and ground-based observations, especially in related to elevated convective snowfall and mixed–phase precipitation, remains limited. Much works need to be done to understand the microphysical mechanisms of spring snowstorms with thunderstorm. Based on multi-source observation data, an in–depth analysis of a spring snowstorm event accompanied by elevated thunderstorm occurred on March 16, 2023 was conducted in this paper. The investigation focuses on cloud microphysical characteristics, the distribution of hydrometeor phases, and the vertical evolution of precipitation parameters, aiming to enhance the understanding of cloud microphysical characteristics and physical mechanisms in snowfall systems.

## 2 Methods and data

### 2.1 Overview of the flight experiment

This study utilizes comprehensive observation data from a field experiment conducted on March 16, 2023. On that day, under the combined influence of the upper–level trough, the low–level shear line, and cold air, a significant precipitation event occurred in the North China Plain. A widespread stratiform–convective mixed clouds moved from southwest to northeast along with the low vortex, affecting the North China Plain region. In the central and western parts of Henan Province, moderate to heavy snow occurred on the ground.

Aircraft observations were carried out along the leading edge of the frontal cloud system(Fig.1). The aircraft (King Air–350) took off from Xinzheng Airport at 11:13 (BJT), climbed vertically over the Zhengzhou area to an altitude of 6,700 m. Level–flight detection was carried out over the Zhengzhou, Xuchang, Pingdingshan, and Zhumadian during 11:43–13:50.

In the study area, two S-band dual-polarization Doppler radars are located in Luoyang (LY, 34.56° N, 112.45° E, elevation 277 m) and Zhengzhou (ZZ, 34.70° N, 113.70° E, elevation 107 m) radar stations. Shangqiu (SQ, 34.44° N, 115.54° E, elevation 47 m) station is equipped with a MRR, a Millimeter–wave Cloud Radar (MCR), and a Microwave Radiometer (MWR). Automatic weighing rain gauges (RGs) from the surface automatic stations are co–located with the MRR, MCR and MWR in this experiment. L–band soundings were daily launched at 08:00 from a site approximately 4 km

https://doi.org/10.5194/egusphere-2026-1706
Preprint. Discussion started: 4 May 2026


from the ZZ radar station and Nanyang station(NY, 33.10° N, 112.48° E, elevation 182 m) to profile the atmospheric vertical structure.

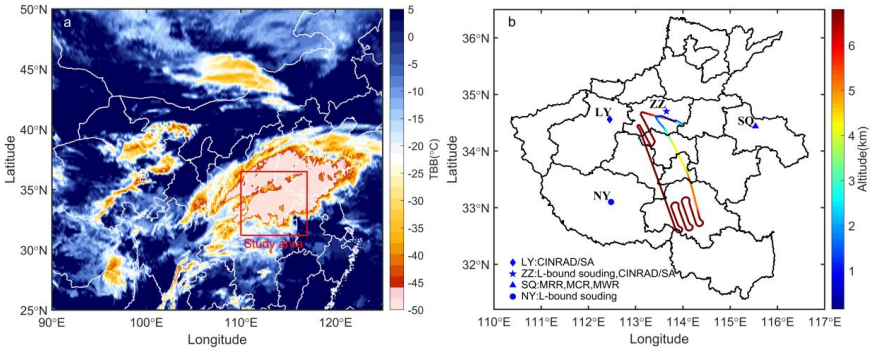


Figure 1. (a) FY–4A infrared blackbody temperature (TBB) image at 11:00 on 16 March 2023. (b) Distribution of instruments in the study area and flight track on March 16, 2023. The color along the flight track represents the aircraft observation altitude.

2.2 Instrument data source

The data used in this study include airborne in situ measurements, L–bound sounding data, rain gauge (RG), MRR, MCR and MWR data from SQ station, and S–band dual-polarization radar data with a temporal resolution of 6 minutes from the ZZ and LY station(Song, 2026). Data from a suite of instruments onboard the aircraft was utilized including an Aircraft-Integrated Meteorological Measurement System (AIMMS), a Cloud Droplet Probe (CDP), and a Cloud Imaging Probe (CIP) from the Droplet Measurement Technologies (DMT), and an airborne Ka–Band Precipitation cloud Radar (KPR). A summary of technical features of the instruments used here is given in Table 1.

Table 1. The instrument used in this study

| Instrument | Variables detected | Measurement range |
|---|---|---|
| AIMMS–20 | Aircraft position and meteorological parameters (height,temperature,humidity, et al) | – |
| CDP | Cloud particle size distribution | 2–50 μm |
| CIP | Cloud particle size distribution and image | 25–1550 μm |
| KPR | Radar reflectivity factor, doppler velocity, Spectrum width | – |
| MRR(24 GHz) | Radar reflectivity factor, doppler velocity, Spectrum width | 100–3100 m(with a vertical resolution of 100 m) |
| MCR(35 GHz) | Radar reflectivity factor, doppler velocity, Spectrum width | ~15 km (with a vertical resolution of 30 m) |
| MWR | Humidity and temperature profile, Total column water vapor, Liquid water path | ~10 km (with a vertical resolution of 30 m) |
| RG | Surface precipitation | |

The data from MRR used in this study include raw data files with spectral Doppler density data and averaged product data. The temporal resolution of the raw data is 10 seconds, while the averaged product data has a temporal resolution of 1 minute. The MCR data has a temporal resolution of 5 s. The temporal resolution of the MWR data is approximately 3–4 minutes. RG provide minutely precipitation data.

https://doi.org/10.5194/egusphere-2026-1706
Preprint. Discussion started: 4 May 2026


2.3 Data processing

To minimize the impact of shattered fragments caused by collisions of ice crystals with the airborne probes under high–speed flight, the CIP data were carefully post–processed using the University of Illinois/Oklahoma Optical Array Probe Processing Software (UIOOPS). Following the methodology of (Mcfarquhar et al., 2018), shattering artifacts were removed based on particle inter–arrival time and aspect ratio and the dimensions of non–complete particles were corrected. The corrections for out of focus particles following Korolev (2007). Due to the large uncertainties for small size particles in the probe's depth of field(Baumgardner and Korolev, 1997), particles with D < 50 μm for the CIP were excluded in this study.

Based on CIP observation, the shape of each individual particle was identified and classified according to the geometric features of precipitation particles. Particles are categorized into 9 types including spherical, tiny, oriented, irregular, aggregates, hexagonal, graupel, linear, and dendrite (Holroyd, 1987; Wang et al., 2023b). A minute–by–minute statistical analysis of particle shapes is conducted to obtain the frequency distribution of particle shapes.

The power spectrum processing method proposed by Garcia-Benadi et al. (2020) was adopted to perform quality control and phase classification of MRR.

For the dual–polarization radar data, the hydrometeor phase was retrieved based on the fuzzy logic algorithm proposed by Dolan et al. (2013).

**3 Results and discussions**

The precipitation was concentrated mainly between 00:00 and 23:00 on March 16. Heavy snow to blizzard conditions were reported in central and western Henan, accompanied by significant lightning activity. With the passage of the cold air mass, temperatures dropped continuously. The rain–snow transition advanced from west to east across the region.

3.1 Microphysical characteristics of cloud based on aircraft detection

As shown in the Fig. 2a, the radar echo top height over the flight area ranged from 8 to 10 km, the base of the echo is located at approximately 1.5 km. The aircraft conducted horizontal flight observations in the middle–upper layers of the cloud. The cloud microphysical characteristics across different periods are analyzed based on in situ aircraft observations.

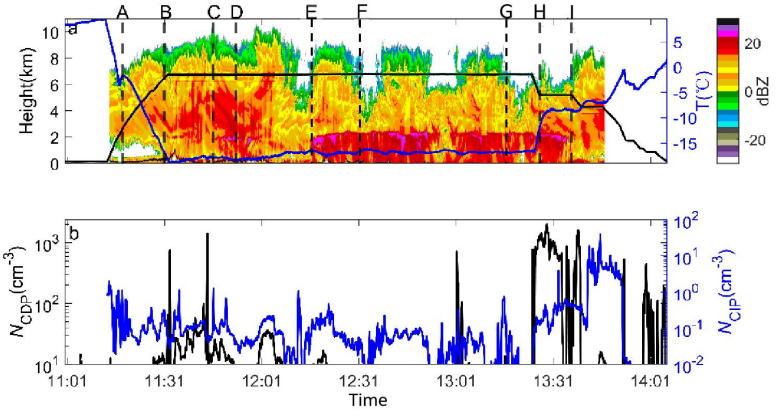


Figure 2. (a) Radar reflectivity from the KPR obtained on March 16, 2023, overlaid with the flight altitude (black solid line) and ambient temperature (blue solid line). (b) the temporal evolution of the number concentration from CDP (black line) and CIP (blue line). A, B, C, D, and E, F in the figure

https://doi.org/10.5194/egusphere-2026-1706
Preprint. Discussion started: 4 May 2026


correspond to the start and end points of the cross-section marked in Fig. 6a,c,e, respectively.

The first stage is from point A (11:18) to point B (11:30). At this stage, the aircraft climbs to the operational altitude in the ZZ area. The flight altitude was between 2622 m and 6500 m (with a corresponding temperature range of −1.7 to −16.9 ℃). The average number concentration observed by the CDP was 3.1 $cm^{-3}$, and the average number concentration observed by the CIP was 131.1 $L^{-1}$. (Table 2). It is evident that during this period, ice crystals dominated the particle population throughout the entire cloud layer. The average liquid water content was below 0.001 g $m^{-3}$, indicating the virtual absence of liquid water in the cloud. The particle size and shape distributions showed little variation with altitude. Deposition and aggregation are important processes for snow growth.

Stage 2 is from point B (11:30) to point D (11:52). The precipitation type at the surface is snow in this stage. Heavy snowfall was observed in this area. The flight altitude of this stage was maintained at approximately 6760 m. The average number concentration measured by the CDP reached 36.7 $cm^{-3}$, while that measured by the CIP was 134.3 $L^{-1}$. Overall, the concentration of small-sized particles observed by CDP was relatively low, while a large number of large-sized ice-phase particles were detected by CIP. A higher content of supercooled water (~0.003 g $m^{-3}$) persists at −18℃ in the upper levels of the cloud layer in this regions.

Stage 3 is between 12:14 and 13:09 (E–G). Mixed precipitation was observed at the surface in this Stage. The aircraft penetrated clouds three times over ZMD at an altitude of 6782 m. Although the detection altitude in this stage was the same as that of Stage 2, the physical parameters exhibited significant differences compared to the previous segment. Compared to the Stage 2, there was a slight reduction in the echo top height measured by the KPR. Meanwhile, a distinct bright band was observed at an altitude of 1.7 km. Both the liquid water content and the particle number concentration observed by the CDP showed a significant decrease.

Stage 4 is between 13:27–13:36 (H–I). The aircraft descended to an altitude of 5215 m to conduct level-flight observations over the ZMD, southern Henan Province. During this stage, the ambient temperature was approximately −8.8 ℃. Compared with the previous three stages, all physical parameters exhibited a substantial increase. Specifically, the particle number concentration measured by the CDP increased by one to two orders of magnitude, while the liquid water content rose by two to three orders of magnitude. The particle concentration from the CIP was of the same order of magnitude as that in Stage 1 and Stage 2, but its value was approximately three times higher than those stages.

Table 2. Physical parameters measured by aircraft at various stages

| | Height(m) | T(℃) | Mean $N_{CDP}$ ($cm^{-3}$) | Mean $N_{CIP}$ ($L^{-1}$) | Mean LWC(g $m^{-3}$) |
|---|---|---|---|---|---|
| 11:18-11:30 (A–B) | 2622–6500 | −16.9~−1.7 | 3.1 | 131.1 | 0.0009 |
| 11:30-11:52 (B–D) | 6752 | −18.1 | 36.7 | 134.3 | 0.003 |
| 12:14-13:09 (E–G) | 6782 | −16.8 | 5.0 | 73.8 | 0.0009 |
| 13:27-13:36 (H–I) | 5215 | −8.8 | 730.8 | 376.3 | 0.15 |

Studies have shown that in shallow convective snow clouds over the Sea of Japan, the maximum cloud droplet concentration reaches 1000 $cm^{-3}$, while 2D-C (2-dimensional cloud particle optical array probes) and 2D-P (2-dimensional precipitation particle optical array probe) particle concentrations

https://doi.org/10.5194/egusphere-2026-1706
Preprint. Discussion started: 4 May 2026


range from 0.6 to 40 $L^{-1}$(Murakami, 2019). Compared to the shallow convective snow clouds over the Sea of Japan, the snow cloud system in this study contains fewer small cloud particles but exhibits higher concentrations of larger ice crystal particles. Similar to the findings ofin the Beijing area (Ma et al., 2021; Gao et al., 2020), the supercooled water content in this snow cloud system is generally low, with sublimation and aggregation serving as the primary microphysical processes. Riming only gradually becomes significant when the supercooled water content is relatively high.

During the first three stages, the mean particle concentration from CIP was 88.2 $L^{-1}$, of which the concentration of small particles in the size range of 75 μm < D < 100 μm was 55.1 $L^{-1}$. All these ice crystals smaller than 100 μm were tiny particles. Statistical results of particle shapes indicate no significant differences in the distribution of particle shapes across different stages (Fig.3). Particles excluding the tiny particles observed by CIP were primarily hexagonal and irregular, accounting for approximately 75% of the total, which is consistent with the research results of Wang et al. (2023b) in East China. In contrast, the concentrations of graupel, linear, oriented and aggregate particles were very low. Compared with dendrite and linear crystals, hexagonal ice crystals are less prone to aggregation, thus inhibiting the formation of aggregates. This explains why few aggregated ice crystals are observed at higher levels (Fig.3b,c) along with a reduction in irregular ice crystals. In contrast, dendrite, aggregated, and irregular ice crystals show an increase at lower levels (Fig.3a). A small number of large supercooled droplets still exist within the cloud. The proportion of spherical particles remained consistently below 10% in Stage 1. The proportion of spherical particles in the Stage 2 and Stage 3 ranged between 10% and 20%, showing an increase compared to the first stage. The particle shape distribution in Stage 4 indicate that almost all of the particles are identified as tiny. Combined with the CIP particle images from this stage, we consider that the observations from the CIP during this period were anomalous, potentially caused by the probe tip freezing upon passing through a supercooled water region.

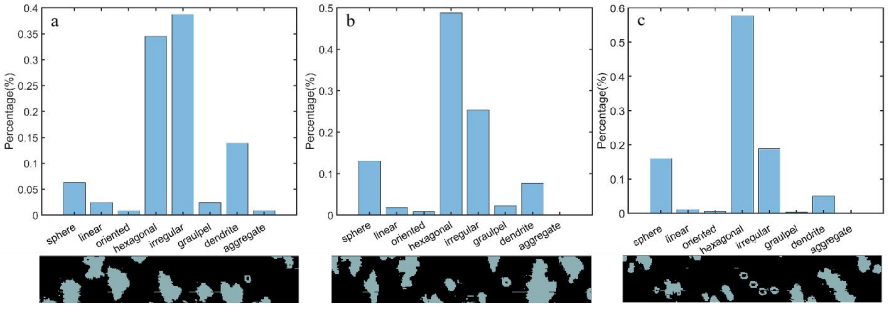


Figure 3. Particle shape distributions observed by airborne CIP at 11:24 (a), 11:48 (b) and 12:42 (c) on March 16, 2023. Particle image from CIP at typical times of different stages are shown under the figure of shape distribution.

In Stage 1, the CDP spectrum exhibited a unimodal distribution, with particle concentrations across all size bins being significantly lower than those in other periods. In contrast, the CIP spectrum showed a distinct bimodal distribution, with peak positions at 75 μm and 375 μm respectively. During this stage, the particle concentrations across all size bins of the CDP showed an increase. In contrast to the previous stage, the CDP spectral distribution in Stage 2 exhibited a bimodal pattern, with the second peak located at 11.5 μm. The spectral distribution from the CIP remained largely consistent with that of Stage 1. The spectral distributions of both the CDP and the CIP in Stage 3 were similar to those

https://doi.org/10.5194/egusphere-2026-1706
Preprint. Discussion started: 4 May 2026


observed in Stage 2. However, the concentration of small particles below 5 μm measured by the CDP showed a significant decrease compared to Stage 2, resembling the levels seen in Stage 1. Since small droplets contribute substantially to the total number concentration, the overall CDP number concentration in this stage was relatively low, accompanied by a reduced liquid water content. In Stage 4, the particle number concentration across all size bins measured by the CDP increased by approximately two orders of magnitude compared to the other three stages. Similar to Stages 2 and 3, the CDP spectral distribution exhibited a multimodal pattern. In contrast, the spectral distribution from the CIP showed distinct differences from the other three stages, primarily manifested as a significant decrease in the number concentration of particles larger than 200 μm.

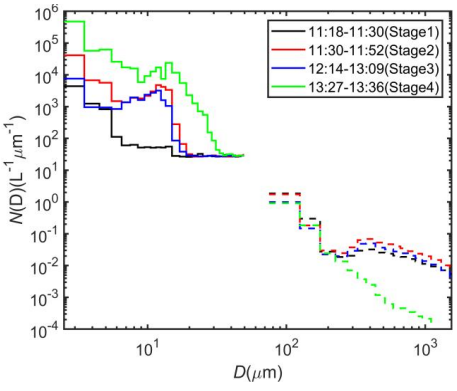


Figure 4. Particle size distributions across different stages. The solid and dashed lines correspond to the CDP and CIP spectra, respectively.

The vertical profiles of radar reflectivity observed by KPR in Stage 1 shows a notable difference compared to the other three stages (Fig.5). Below 3 km in Stage 1, there is a distinct decrease in radar reflectivity. The radar reflectivity below 1.5 km in the lower layer is less than 10 dBZ. The sounding profiles from ZZ at 08:00 reveal a relatively dry lower troposphere, with relative humidity below 60% beneath 1.4 km. The low relative humidity in the lower levels leads to the evaporation of precipitation particles during their descent, resulting in a decrease in radar reflectivity. Within the cloud, radar reflectivity increases as altitude decreases. However, the doppler velocity and the spectral width shows a distinct decreasing trend.

The vertical profiles of radar reflectivity, doppler velocity, and spectral width are similar in Stage 3 and Stage 4. The radar reflectivity revealed a pronounced enhancement at an altitude of 1.8 km, which is likely associated with the melting layer where ice particles begin to melt. Within the melting layer, the radar reflectivity intensifies, accompanied by a decrease in velocity. Below the melting layer (0°C isotherm), both the doppler velocity and velocity spectral width continue to increase. In contrast, the radar reflectivity factor tends to decrease with decreasing height. Ice crystals melt into spherical raindrops, their air resistance decreases, leading to a significant increase in their fall speed under gravitational acceleration. When the ice core completely disappears and transforms into droplets, their size decreases compared to snowflakes coated with a water film. Meanwhile, the particle number concentration decreases as the fall speed increases. This results in the observed reduction in the radar reflectivity.

During the stage of snowfall observed at the surface (Stage 2), radar reflectivity above the 0 °C level are significantly larger compared to other Stages, indicating that the snowflakes in the upper

https://doi.org/10.5194/egusphere-2026-1706
Preprint. Discussion started: 4 May 2026


layers of the cloud system are significantly larger than those in other areas. However, below the 0 °C level, the radar reflectivity during this Stage is weaker than Stage 3 and 4. This is primarily due to the increase in the dielectric constant of the particles after melting.

Among all stages, with increasing altitude, the radar reflectivity and doppler velocity decrease sharply, while the spectral width increases significantly near the cloud top. This indicates that under the influence of the evaporation and entrainment, particle size decreases, but the size distribution broadens.

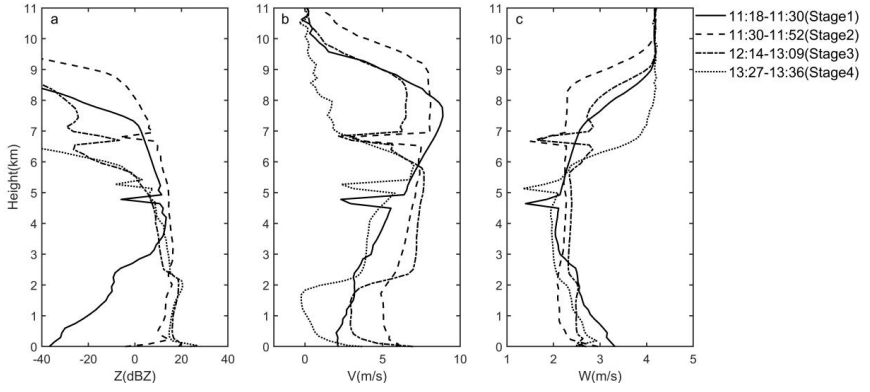


Figure 5. Vertical profiles of radar reflectivity(a), doppler velocity(b), and velocity spectrum width(c) observed by the KPR of different Stages.

3.2 Analysis of vertical distribution of hydrometeor

The detection coverage of airborne observations is limited as its altitude is primarily maintained at the the operational altitude. Therefore, supplementary analysis were conducted based on the observations from the dual–polarization radar to gain deeper insights into the vertical structure of precipitation and the evolution characteristics of hydrometeor phases.

Radar reflectivity images at 0.48° elevation angles (Fig. 6a,c,e) depict widespread stratiform clouds embedded with convective cells over central and western Henan, with a maximum reflectivity of 45 dBZ. To investigate the vertical structure of the precipitation, a cross–sectional analysis of the S–band dual–polarization radar echoes near the time of the aircraft's flight was performed along the flight track. The black solid line(from A to B, C to D, E to F in Fig. 6a,c,e) indicates the positions of cross–section, which largely coincides with the aircraft's flight path at the respective time.Ten precipitation particle phases, namely large droplets, hail, high–density graupel, low–density graupel, vertical ice crystals, wet snow, ice crystals, aggregates, rain, and drizzle, were classified based on the radar-observed parameters including reflectivity (Z), specific differential phase (KDP), differential reflectivity (ZDR), and correlation coefficient (CC) (Dolan et al., 2013).

At 11:24, the precipitation particles over ZZ were dominated by wet snow and aggregates. with droplets and low–density graupel present in the lower troposphere (below 3 km) near Point B, where radar reflectivity is relatively strong. (shown in Fig. 6a, b).

The vertical distribution of particle phases at 11:48 shows a marked difference compared to that at 11:24. At 11:48, the precipitation particles in the 6−8 km layer were wet snow, aggregates and vertical ice crystals. Meanwhile, supercooled water exists between 3 and 5 km.Within this altitude range, supercooled droplets collide with ice crystals and freeze through the riming process, forming graupel particles. High−density graupel, low−density graupel were the dominant particle types below 3 km.

At 12:18, the radar cross-section indicates that the vertical distribution characteristics of

https://doi.org/10.5194/egusphere-2026-1706
Preprint. Discussion started: 4 May 2026


hydrometeor phases in the cloud system over the Pingdingshan area are similar to those over the ZZ region. Throughout the entire layer, particles consist predominantly of wet snow and aggregates, accompanied by a small amount of vertical ice crystals. In areas of higher reflectivity, supercooled liquid droplets are present around the 3 km level in the mid–levels.

As evident from the above analysis, there is a marked difference in the vertical distribution of particle phases between the convective regions with higher radar reflectivity and the surrounding stratiform cloud regions. Studies have shown that graupel particles are the key factor for electrification (Zhou and Guo, 2009; Kumjian and Deierling, 2015). In convective regions with strong radar reflectivity, vertical airflows enhance particle collision processes. Collisions between graupel particles and ice crystals generate surface contact potential differences, leading to charge transfer between the particles. As a result, the two types of particles carry opposite electrical charges. The heavier graupel particles descend to the middle–lower part of the cloud, while the lighter ice crystals are carried to the upper layers by updrafts (see Fig. 6 b,d), forming a dipolar structure. This non–inductive electrification mechanism is responsible for the thunderstorm events observed over central Henan(Jayaratne et al., 1983; Reynolds et al., 1957; Saunders et al., 1991).

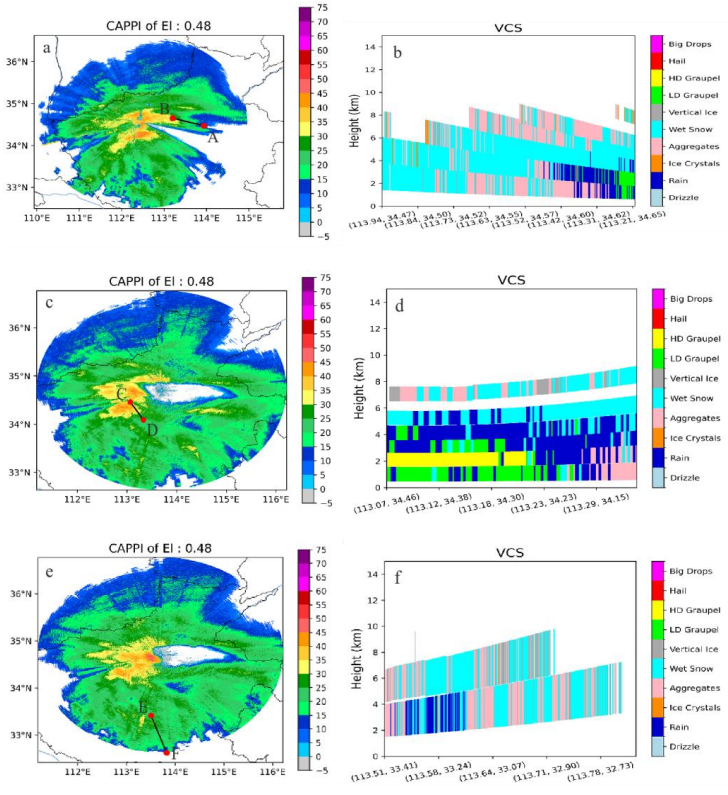


Figure 6. CAPPI (Constant Altitude Plan Position Indicator) images at a 0.48° elevation angle from (a) LY radar at 11:24, (c) ZZ radar at 11:48, and (e) ZZ radar at 12:18 on March 16, 2023. The black solid lines in the images indicate the cross-section positions, with red scatter points A, B and C, D marking the start and end points of the cross-section profiles. Panels (b), (d), and (f) display the corresponding cross-section profiles of precipitation type for 11:24, 11:48, and 12:18 respectively.

https://doi.org/10.5194/egusphere-2026-1706
Preprint. Discussion started: 4 May 2026


According to the S-band dual-polarization radar observations, over the ZZ area the dominant hydrometeor types consisted of wet snow and aggregates, while a similar composition is observed at higher levels (6−8 km) in the LY area. Analysis of the airborne particle images reveals that the cloud was primarily composed of hexagonal and irregular ice crystals. Although there are some discrepancies between airborne and dual-polarization radar classifications of particle types, both observational results indicate that in relatively stable stratiform cloud regions, the precipitation particles is predominantly composed of ice crystals with low supercooled water content. In contrast, within areas of stronger radar reflectivity associated with convection, the mid–levels contain abundant supercooled water. Under the influence of riming and non-inductive charging processes, particles undergo significant growth through collision and coalescence, leading to pronounced lightning activity.

### 3.3 Vertical precipitation structure and phase evolution in the SQ region

Compared to the central and western parts of Henan Province, snowfall in the eastern region occurs later and is significantly weaker. In this section, a detailed analysis of the precipitation vertical structure based on ground-based vertical ground−based observations at the SQ station are provided.

Between 00:00 and 06:00, the cloud base height was remained around 3 km. From 10:00 onward, the cloud system developed and deepened, cloud base height began to descend continuously until 14:00. The top height of radar reflectivity reached approximately 12 km, showing a strong vertical development (Fig. 7a). Although precipitation echoes developed below 3 km after 11:00, no precipitation was recorded at the ground prior to 14:00. This absence of surface rainfall can be attributed to dry layers located between 2−3 km and below 1.5 km (Fig. 7c). As precipitation particles descended through these dry layers in the lower troposphere, they evaporated due to the low humidity, ultimately failing to reach the surface. Under the effect of phase-change cooling, the near-surface temperature further decreases.

Starting at 14:00, the radar echoes reached the ground, marking the beginning of surface. Approximately half an hour before the surface precipitation formation (around 13:30), both the ILW and IWV values exhibited a sharp increase, accompanied by a notable increasing relative humidity of the lower troposphere (Fig.7d). This phenomenon is consistent with findings from previous studies(Lei et al., 2001; Zhang and Zhou, 2010), demonstrating the IWV and ILW from MWR provide valuable early indications of impending precipitation. As shown in the temperature and humidity profile from the ERA5 grid point nearest to SQ station (Fig. 7c), moisture was predominantly concentrated below 600 hPa after precipitation onset at 14:00, with a distinct layer of low relative humidity between 400 and 600 hPa.

We divided the precipitation process into three stages (as shown in Fig. 7) based on the evolutionary characteristics of the radar reflectivity. The first stage of precipitation is from 14:00 to 16:00. The radar reflectivity shows significant enhancement below 0.5 km, the surface temperature decreased from 6.4 °C to 3.8 °C. The second stage of precipitation is from 16:00 to 18:00. During this stage, the radar echo intensity was relatively high below 2 km and the 0 °C level height shows no significant change. The last stage of precipitation is from 18:00 to 23:00, during this stage, the radar reflectivity was relatively low overall. After 21:00, both the surface temperature and the height of the 0℃ isotherm decreased noticeably with the passage of cold air.

https://doi.org/10.5194/egusphere-2026-1706
Preprint. Discussion started: 4 May 2026


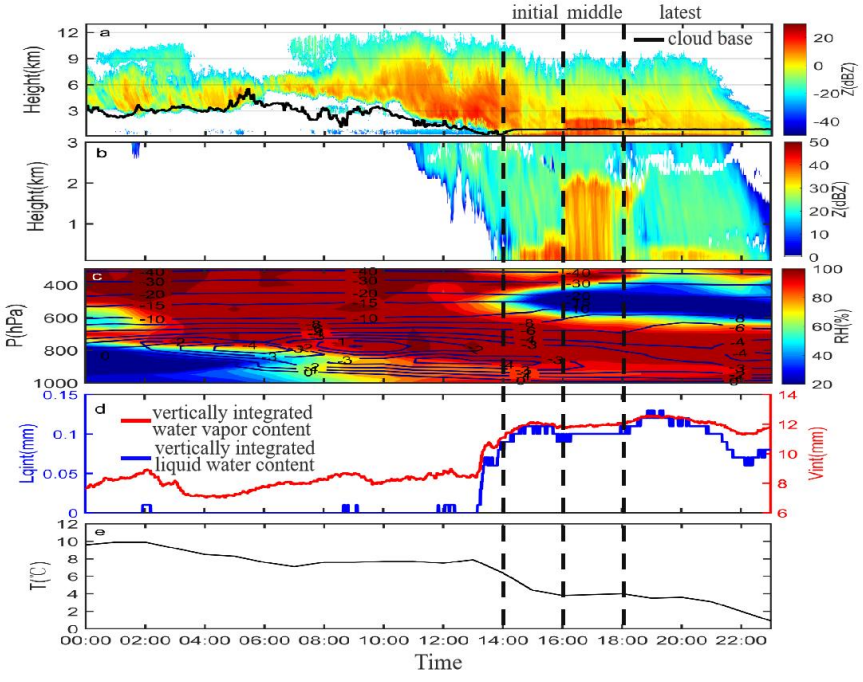


Figure 7. (a) Radar reflectivity observed by the MCR, (b) radar reflectivity observed by the MRR, (c) temporal evolution of vertical relative humidity distribution from ERA5, (d) vertically integrated liquid water content (Lqint) and vertically integrated water vapor content (Vint) from MWR and (e) surface temperature at the SQ station on March 16, 2023. The cloud base height observed by the MWR is indicated by the black solid line in subplot a. 1,2,3 represent three stages of the precipitation.

To understand the differences in the vertical structure of precipitation during different rainfall periods, we analyzed the Contoured Frequency by Altitude Diagrams (CFADs) (Yuter and Houze, 1995) of the equivalent radar reflectivity factor ($Z_e$), doppler velocity ($V$) and spectrum width ($W$) profiles in this section.

As illustrated in the Fig. 8, during the initial precipitation period, $Z_e$ above 1 km exhibits a relatively narrow distribution, with values predominantly ranging between 20 and 30 dBZ and an average of approximately 23 dBZ. As altitude decreases, the distribution of $Z_e$ broadens. Meanwhile, high-frequency interval of $Z_e$ shifts toward higher values. Below 0.5 km, $Z_e$ shows a noticeable increasing trend. The $W$ exhibited a showed a similar vertical profile as $Z_e$. The $V$ showed a increasing trend descending from 3 km to 2 km, whereas it exhibited no pronounced variation between 2 km and 1 km. Below 1 km, $V$ showed a clear increasing trend.

Unlike the initial precipitation period, during the mid-precipitation stage, $Z_e$ ranges from 12 to 30 dBz with the highest occurrence frequency around 24 dBz above 2.4 km. Between 2.4 km and 1.8 km, $Z_e$ shows a significant increasing trend as altitude decreases. Below 1.8 km, $Z_e$ has the highest probability of occurring at 36 dBz while the mean $Z_e$ value exhibits no obvious changing trend. $Z_e$ shows no significant variation below 1.8 km, indicating that raindrop coalescence is not pronounced in these layers. The precipitation intensity is low and the spectral reflectivity width is narrow in this stage, resulting in insignificant raindrop coalescence. Above 2.1 km, $V$ showed insignificant variation. A local

https://doi.org/10.5194/egusphere-2026-1706
Preprint. Discussion started: 4 May 2026


minimum in $V$ was present around 1.7 km. Below 1.4 km, the absolute value of $V$ demonstrated a clear increasing trend, which differed from that of $Z_e$. The $W$ exhibited a pronounced maximum around 2 km, with a slight increasing trend observed below 1.7 km.

During the late precipitation period, the average value of $Z_e$ is minimal in the upper layers (approximately 18 dBZ). Between 2.5 km and 0.5 km, the average $Z_e$ initially increases and then decreases with decreasing altitude, with a weak peak at around 1.8 km. The highest frequency of $Z_e$ occurrence consistently lies within the 20–24 dBZ range. The velocity profile from the MRR shows positive values around 1.5 km, suggesting that light snowflakes with low density, were likely being lifted by relatively strong updrafts. An analysis of the vertical velocity from the nearest ERA5 reanalysis grid point to the SQ station reveals that around 19:00, the vertical velocity at 850 hPa was approximately −0.7 Pa/s, confirming the presence of ascending motion near that altitude. Within this updraft, snow particles accumulated and grew, leading to a localized $Z_e$ enhancement above this layer. Similar to the early precipitation stage, $Z_e$ in the lower layers (below 0.5 km) during the later stage also shows a distinct increasing trend.

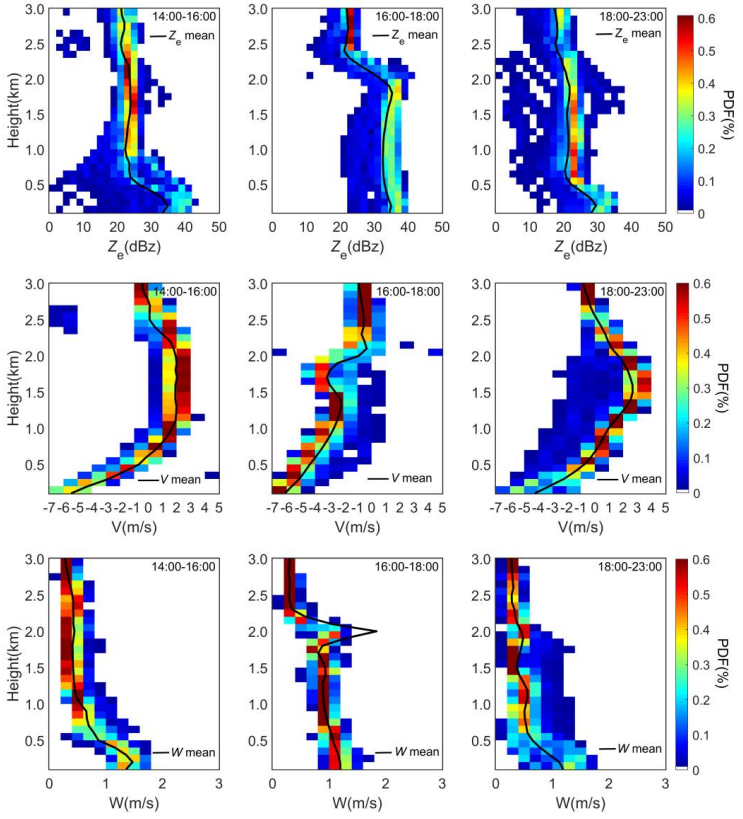


Figure 8. Vertical frequency distribution of equivalent reflectivity factor ($Z_e$), doppler velocity ($V$) and spectrum width ($W$) derived from the MRR observations at the SQ station on March 16, 2023, for the periods 14:00–16:00, 16:00–18:00, and 18:00–23:00.

The precipitation phase retrieval method proposed by Garcia-Benadi et al. (2020) was applied to investigate the vertical transition of hydrometeor phases across different stages.

According to phase identification results, during the initial precipitation period, a mixed phase of

https://doi.org/10.5194/egusphere-2026-1706
Preprint. Discussion started: 4 May 2026


precipitation was observed near the ground (below 0.5 km), while the upper levels consisted of pure snow. As the precipitation particles descended through a near–surface layer with temperatures above 0 °C, they gradually melted into mixed phase. Since the dielectric constant of water is greater than that of ice, leading to a significant enhancement of the radar reflectivity in the lower layers.

A temperature inversion layer was identified within the 850–750 hPa (Fig.7c). This presence of an inversion layer is further corroborated by the 20:00 radiosonde profiles from the three stations near the SQ station (Table 3). The analysis of radiosonde observations reveals that, although the temperature profiles from the three sounding stations share similarities, substantial differences exist in both the specific temperature values and the height of the 0 °C level. ZZ station, located the furthest west, experienced the earliest cooling. Consequently, despite the presence of an elevated temperature inversion, no warm layer (layer with temperature over 0 °C) existed throughout the entire atmospheric column at this site. In contrast, due to the existence of the temperature inversion, distinct warm layers were observed at Fuyang and Xuzhou stations within the altitude ranges of 1509−2042 m and 1945−2660 m, respectively. The thicknesses of these warm layers were approximately 533 m and 715 m for Xuzhou and Fuyang.

During the mid–precipitation stage, precipitation particles converting from pure snow to mixed between 2.1 km and 1.5 km during this stage, which results in a notable increase in $Z_e$. The presence of a warm, moist inversion layer was the main reason for the melting of precipitation particles. With further descent, precipitation particles turn into a pure liquid phase in the lower layers (below 0.7 km).

During the late precipitation period, the vertical distribution of precipitation particles phase before 22:00 resembled that observed in the initial stage, with mixed–phase precipitation occurring near the surface (below 0.5 km) and pure snow present aloft. The melting and aggregation of snowflakes remain the main reason for the increase in echoes below 0.5 km in the lower layers as height decreases. Additionally, a region with negative vertical velocity and unclear precipitation phase existed between 1 km and 2 km during 18:46–22:00, which might be related to strong updrafts. After 22:00, the precipitation phase transitioned to snow in all layers.

Although surface temperatures were above 0°C during both the initial and final stages of precipitation, the observed surface precipitation types were mixed–phase or pure snow, indicating that the ice–phase particles formed at higher altitudes were not completely melted as they passed through the warm layer. Existing subjective precipitation type classification primarily relies on temperature thresholds at key atmospheric levels. The 925 hPa temperature below −2 °C (Xu et al., 2006), 1000 hPa temperature below 2 °C, and surface air temperature near 0 °C (Li et al., 2009) have been conventionally used as discrimination criteria for rain-snow phase transition. In the early stage of precipitation in this study, although the 925 hPa temperature was below −2 °C, the surface temperature was significantly above 0 °C, indicating a pronounced vertical temperature contrast with colder mid-levels and warmer surface conditions, resulting in mixed-phase precipitation at the surface. Statistical research by Peng et al. (2015) on precipitation types in Zhejiang Province demonstrated that sleet events occur within a surface temperature range of 0.2–6.6 °C. The surface temperatures during sleet occurrences in this study are generally consistent with findings in Zhejiang. During the mid-stage of precipitation, despite lower surface temperatures compared to the initial stage, the observed surface precipitation type was rain, suggesting that relying solely on surface temperature for precipitation type diagnosis may introduce certain inaccuracies.

Additionally, thickness indices such as the 850–700 hPa and 1000–850 hPa layers have also been applied in snowfall identification analyses. Xu and Zong (2014) indicated that when the thickness

https://doi.org/10.5194/egusphere-2026-1706
Preprint. Discussion started: 4 May 2026


difference between 850 hPa and 1000 hPa is less than 1300 gpm, and the thickness difference between 700 hPa and 850 hPa is less than 1530 gpm, the surface precipitation type is predominantly snow or sleet; otherwise, rain prevails. In this case, from 14:00 to 22:00, the geopotential height differences for both the 850−700 hPa and 1000−850 hPa layers continuously decreased. During the middle stage of the precipitation event, the 850−700 hPa and 1000−850 hPa thickness differences are below 1530 gpm and 1300 gpm, respectively. The precipitation phase can't be correctly identified by applying previous thresholds. Therefore, although surface temperature and characteristic-layer thickness differences can serve as criteria for phase discrimination, the threshold values for these indicators require further region−specific investigation. In addition to temperature and thickness between characteristic layer, cloud microphysical features such as hydrometeor types also influence the phase transition during hydrometeor descent, thereby affecting the surface precipitation type. These factors should be comprehensively considered in precipitation−phase forecasting.

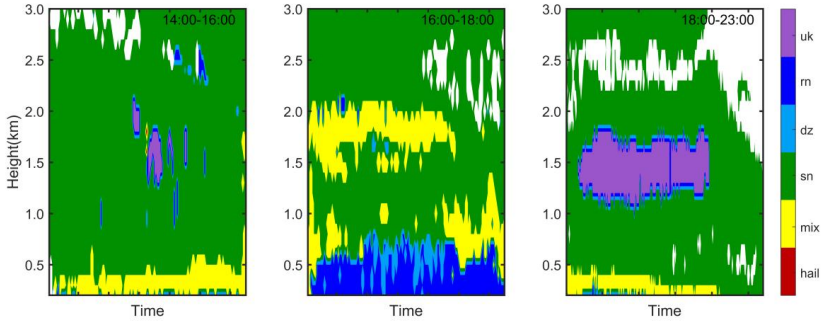


Figure 9. Vertical distribution of precipitation phase derived from the MRR observations at the SQ station on March 16, 2023, for the periods 14:00−16:00, 16:00−18:00, and 18:00−23:00.

Table 3. Vertical structure from radiosonde observations at Zhengzhou, Xuzhou, and Fuyang stations at 20:00 on 16 March 2023

| | Zhengzhou | Xuzhou | Fuyang |
|---|---|---|---|
| Height of the 0 °C Level(m) | 313 | 753 | 1067 |
| Temperature inversion layer (m) | 2290−2689m(−6.4–−2.8) | 1355-1696m(−1.7–2.5) | 1775-2187m(−2.6–2.6) |
| Warm layer (m) | / | 1509−2042 | 1945−2660 |
| Thickness of warm layer (m) | / | 533 | 715 |

The phase of precipitation significantly affects the accuracy of radar quantitative precipitation estimation(Huang et al., 2015; Cifelli et al., 2011; Mai et al., 2023). As shown, the precipitation intensity derived from the original minute−level products of the MRR provided by Meteorologische Messtechnik GmbH (METEK) was significantly higher than the measurements from the automatic surface station during the periods of 14:00−16:00 and 20:00−22:00. In contrast, the precipitation intensity values from both sources were in close agreement when surface precipitation was predominantly liquid between 16:00−18:00 (Fig. 10).This discrepancy stems from the assumption in the MRR retrieval algorithm(detailed in the MRR Physical Basics(2012)) of a specific relationship between the falling velocity and particle size of liquid precipitation particles (Peters et al., 2005). As a result, the original MRR products are inherently optimized for liquid precipitation (Wang et al., 2017). The application of this retrieval algorithm to non−liquid phases, such as snowfall, introduces notable errors.

https://doi.org/10.5194/egusphere-2026-1706
Preprint. Discussion started: 4 May 2026


Snowfall intensity is usually estimated using the empirical formula $Z_e=a\cdot SR^b$ (Kneifel et al., 2011; Souverijns et al., 2017; Matrosov et al., 2009), where $Z_e$ denotes the effective radar reflectivity factor with units of $mm^6\ m^{-3}$, and SR represents the snowfall rate with units of mm $h^{-1}$. The $Z_e$−SR relationship is highly sensitive to the assumed snow particle shape and particle size distribution, with the coefficients a and b exhibiting a wide range of variability(Kulie and Bennartz, 2009; Matrosov, 2007; Noh et al., 2006). Precipitation intensity was retrieved again using different sets of coefficients. The results indicate that the parameter values for aggregated ice crystals proposed by Kulie and Bennartz (2009) yield more accurate precipitation estimates, whereas the application of parameters from other algorithms (e.g., those for low−density spherical snow particles) leads to a significant overestimation of precipitation intensity. As illustrated in the Fig.10 compared with the precipitation intensity from the original retrieval scheme, the retrieved values optimized based on phase classification show better agreement with the observations from the surface automatic weather station, with the relative error reduced from 5.14 to 0.70.

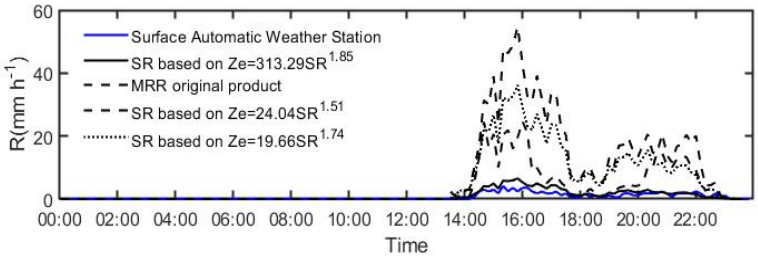


Figure 10. Precipitation intensity from surface automatic station observations, original MRR minute−level products, and snowrate based on $Z_e$−SR relationship at the SQ station on 16 March 2023.

## 4 Conclusions

During this event, the cloud system that produced the snowfall in the North China Plain exhibited a low concentration of small cloud droplets(not exceeding 10 $cm^{-3}$) and a relatively high concentration of large-scale ice crystals (reaching up to 131.1 $L^{-1}$) in the stratiform areas.

The concentration of small cloud droplets in regions with vigorous convective development at the height around 6.8 km (with temperature around − 18 ℃), is significantly higher than in other regions. Additionally, the supercooled water content in these areas is greater, reaching up to 0.003 g $m^{-3}$.

The ice crystal types were mainly dominated by hexagonal and irregular shapes. In regions with stronger radar reflectivity associated with convection, the upper levels were primarily composed of aggregates and vertically oriented ice crystals, the middle layers contained supercooled water, and the lower layers were dominated by graupel particles. Supercooled droplets collide with ice crystals and freeze through the riming process between 3−5 km, forming graupel particles. Influenced by non-inductive charging mechanisms, significant lightning activity occurred in these areas.

Surface precipitation types at the SQ station experienced multiple transitions, shifting from sleet to rain, then back to sleet, and finally to snow. The vertical precipitation structure over the SQ area exhibits distinct characteristics across different stages. During both the early and late stages of the precipitation, snow crystals partially melted near the surface (below 0.5 km), resulting in a distinct increasing trend in the $Z_e$ in the lower layers during these periods. During the middle stage of precipitation, the transition from pure snow to mixed occurred at a higher altitude, leading to a marked increase in $Z_e$ between 2.4 and 1.8 km. The presence of a warm, moist inversion layer provided favorable conditions for the melting of precipitation particles. As the altitude decreased, precipitation

https://doi.org/10.5194/egusphere-2026-1706
Preprint. Discussion started: 4 May 2026


particles in the lower layers (below 0.7 km) became entirely liquid. In the late stage, the presence of an updraft allowed ice crystals to continue growing while being suspended. Meanwhile, updraft prevent precipitation particles from descending, leading to particle accumulation and an increased number concentration within this layer, explaining the localized maximum in $Z_e$ in the updraft region (1.5−2.3 km).

Compared to the precipitation intensity from raw product of MRR, the retrieved precipitation intensity based on $Z_e$−SR relationship shows closer agreement with the measurements from the surface automatic weather station.

The findings from this snowstorm case study provide detailed insights into precipitation phase transitions and the involved microphysical processes based on comprehensive measurements. Additionally, The snowfall intensity estimated by $Z_e$ − SR relationship shows better agreement to automatic weather station observations, providing valuable information for estimations of solid precipitation intensity. However, as precipitation vertical structures and microphysical mechanisms vary significantly across different weather systems, characteristics of more spring snowstorm events remain to be conducted. Only the vertical distribution of radar original parameters and precipitation phase were studied in this research. The particle size distribution (PSD) is important to understanding the microphysical mechanisms. Developing methods to obtain more reliable and realistic PSD by accounting for phase identification could be explored in future research.

## Data availability

The satellite, aircraft and other ground-based data is available at Zenodo (Song, 2026, https://doi.org/10.5281/zenodo.19329115). The ERA5 data is obtained from https://cds.climate.copernicus.eu/datasets (ERA5 hourly data on pressure levels from 1940 to present, last access: 7 September 2025). The L–bound sounding data is available at http://weather.uwyo.edu/upperair/bufrraob.shtml.

## Author contributions

**Can Song:** Methodology, Formal analysis, Investigation, Data Curation, Visualization, Writing - Original Draft, Writing - Review & Editing. **Chong Peng and Honglei Wang:** Conceptualization, Supervision, Writing - Review & Editing. **Ting Bai:** Data Curation, Resources, Validation, Visualization. **Yimei Huang, Jianfang Ding:** Methodology, Resources, Supervision. **Yanhua Liu, Zhenping Shao and Xiuzhu Sha:** Data Curation, Formal analysis, Validation.

## Competing interests

The authors declare that they have no conflict of interest

## Disclaimer

Publication's note: Copernicus Publications remains neutral with regard to jurisdictional claims made in the text, published maps, institutional affiliations, or any other geographical representation in this paper. While Copernicus Publications makes every effort to include appropriate place names, the final responsibility lies with the authors. Views expressed in the text are those of the authors and do not necessarily reflect the views of the publisher.

## Acknowledgements

https://doi.org/10.5194/egusphere-2026-1706
Preprint. Discussion started: 4 May 2026


The authors sincerely appreciate the developers for UIOOPS and Pro.Yang Wang from Lanzhou University for the help with data processing.

**Financial support**

The research was supported in part by Henan Key Laboratory of Agrometeorological Safeguard Application Technique, CMA, Fund Project(China) (project number KQ202425, for Can Song), Henan Provincial Department of Science and Technology/Henan Provincial Key R&D and Promotion Special Project (China) (Grant No. 232102320013, for Jianfang Ding, Grant No. 242102321022, for Ting Bai, Grant No. 252102321006 for Chong Peng and Grant No. 242102320037, for Yanhua Liu).

**References**

Physical Basics: http://www.metek.de, last access: March 13.

Andrews, A., Sumesh, R. K., Resmi, E. A., Sukumar, N., Gopan, G., Anilkumar, L., Kumar, S., Manoj, M. G., Jash, D., and Unnikrishnan, C. K.: Microphysical characteristics of shallow precipitating systems in the southwest monsoon season: An analysis using in-situ and remote sensing observations, Journal of Atmospheric and Solar-Terrestrial Physics, 269, 106484, https://doi.org/10.1016/j.jastp.2025.106484, 2025.

Barthazy, E. and Schefold, R.: Fall velocity of snowflakes of different riming degree and crystal types, Atmospheric Research, 82, 391-398, https://doi.org/10.1016/j.atmosres.2005.12.009, 2006.

Baumgardner, D. and Korolev, A.: Airspeed Corrections for Optical Array Probe Sample Volumes, J. Atmos. Ocean. Technol., 14, 1224-1229, https://doi.org/10.1175/1520-0426(1997)014<1224:ACFOAP>2.0.CO;2, 1997.

Bechini, R. and Chandrasekar, V.: A Semisupervised Robust Hydrometeor Classification Method for Dual-Polarization Radar Applications, J. Atmos. Ocean. Technol., 32, 22-47, https://doi.org/10.1175/JTECH-D-14-00097.1, 2015.

Cha, J.-W., Chang, K.-H., Yum, S. S., and Choi, Y.-J.: Comparison of the bright band characteristics measured by Micro Rain Radar (MRR) at a mountain and a coastal site in South Korea, Advances in Atmospheric Sciences, 26, 211-221, http://doi.org/10.1007/s00376-009-0211-0, 2009.

Cifelli, R., Chandrasekar, V., Lim, S., Kennedy, P. C., Wang, Y., and Rutledge, S. A.: A New Dual-Polarization Radar Rainfall Algorithm: Application in Colorado Precipitation Events, J. Atmos. Ocean. Technol., 28, 352-364, https://doi.org/10.1175/2010JTECHA1488.1, 2011.

Das, S., Shukla, A. K., and Maitra, A.: Investigation of vertical profile of rain microstructure at Ahmedabad in Indian tropical region, Advances in Space Research, 45, 1235-1243, https://doi.org/10.1016/j.asr.2010.01.001, 2010.

Das, S. K., Konwar, M., Chakravarty, K., and Deshpande, S. M.: Raindrop size distribution of different cloud types over the Western Ghats using simultaneous measurements from Micro-Rain Radar and disdrometer, Atmospheric Research, 186, 72-82, https://doi.org/10.1016/j.atmosres.2016.11.003, 2017.

Dolan, B., Rutledge, S. A., Lim, S., Chandrasekar, V., and Thurai, M.: A Robust C-Band Hydrometeor Identification Algorithm and Application to a Long-Term Polarimetric Radar Dataset, J. Appl. Meteorol, Climatol., 52, 2162-2186, https://doi.org/10.1175/JAMC-D-12-0275.1, 2013.

https://doi.org/10.5194/egusphere-2026-1706
Preprint. Discussion started: 4 May 2026


Feng, Q., Niu, S., Hou, T., Yue, Z., and Shen, D.: Aircraft Observations of Characteristics and Growth of Ice Particles of Two Different Snowfall Clouds in Shanxi Province, China, Atmosphere, 12, 477, https://doi.org/10.3390/atmos12040477, 2021a.

Feng, Q., Niu, S., Hou, T., Fan, X., Shen, D., and Yang, J.: Aircraft-Based Observation of the Physical Characteristics of Snowfall Cloud in Shanxi Province, Chinese Journal of Atmospheric Sciences, 45, 1146-1160 (in Chinese). 2021b.

Finlon, J. A., Mcfarquhar, G. M., Rauber, R. M., Plummer, D. M., Jewett, B. F., Leon, D., and Knupp, K. R.: A Comparison of X-Band Polarization Parameters with In Situ Microphysical Measurements in the Comma Head of Two Winter Cyclones, Journal of Applied Meteorology and Climatology, 55, 2549-2574, https://doi.org/10.1175/JAMC-D-16-0059.1., 2016.

Gao, Q., Guo, X., Liu, X. e., and He, H.: Numerical Simulation and Observation Study on Microphysical Formation Processes of Two Different Snowfall Cases in Northern Mountain Area of Beijing, Chinese Journal of Atmospheric Sciences, 44, 407-420 (in Chinese). 2020.

Garcia-Benadi, A., Bech, J., Gonzalez, S., Udina, M., Codina, B., and Georgis, J.-F.: Precipitation Type Classification of Micro Rain Radar Data Using an Improved Doppler Spectral Processing Methodology, Remote Sensing, 12, 4113, http://doi.org/10.3390/rs12244113, 2020.

Geerts, B., Yang, Y., Rasmussen, R., Haimov, S., and Pokharel, B.: Snow Growth and Transport Patterns in Orographic Storms as Estimated from Airborne Vertical-Plane Dual-Doppler Radar Data, Monthly Weather Review, 143, 644-665, https://doi.org/10.1175/MWR-D-14-00199.1, 2015.

He, J., Zheng, J., Zeng, Z., Che, Y., Zheng, M., and Li, J.: A Comparative Study on the Vertical Structures and Microphysical Properties of Stratiform Precipitation over South China and the Tibetan Plateau, Remote Sensing, 13, 2897, http://doi.org/10.3390/rs13152897, 2021.

Holroyd, E. W., III: Some Techniques and Uses of 2D-C Habit Classification Software for Snow Particles, J. Atmos. Ocean. Technol., 4, 498-511, https://doi.org/10.1175/1520-0426(1987)004<0498:STAUOC>2.0.CO;2, 1987.

Hu, Z. and Srivastava, R. C.: Evolution of Raindrop Size Distribution by Coalescence, Breakup, and Evaporation: Theory and Observations, Journal of Atmospheric Sciences, 52, 1761-1783, https://doi.org/10.1175/1520-0469(1995)052<1761:EORSDB>2.0.CO;2, 1995.

Huang, G. J., Bringi, V. N., Moisseev, D., Petersen, W. A., Bliven, L., and Hudak, D.: Use of 2D-video disdrometer to derive mean density–size and Ze–SR relations: Four snow cases from the light precipitation validation experiment, Atmospheric Research, 153, 34-48, http://doi.org/10.1016/j.atmosres.2014.07.013, 2015.

Huang, Y., Zhao, D., Du, Y., Chen, Y., Zhang, L., Li, X., and Jing, Y.: Vertical Structure of a Snowfall Event Based on Observations From the Aircraft and Mountain Station in Beijing, Frontiers in Environmental Science, Volume 9 - 2021, https://doi.org/10.3389/fenvs.2021.783356, 2021.

Jayaratne, E. R., Saunders, C. P. R., and Hallett, J.: Laboratory studies of the charging of soft-hail during ice crystal interactions, Quarterly Journal of the Royal Meteorological Society, 109, 609-630, https://doi.org/10.1002/qj.49710946111, 1983.

Kneifel, S., Kulie, M. S., and Bennartz, R.: A triple-frequency approach to retrieve microphysical snowfall parameters, Journal of Geophysical Research: Atmospheres, 116, https://doi.org/10.1029/2010JD015430, 2011.

https://doi.org/10.5194/egusphere-2026-1706
Preprint. Discussion started: 4 May 2026


667 Korolev, A.: Reconstruction of the Sizes of Spherical Particles from Their Shadow Images.
668 Part I: Theoretical Considerations, Journal of Atmospheric and Oceanic Technology, 24, 376-
669 389, https://doi.org/10.1175/JTECH1980.1, 2007.
670 Kulie, M. and Bennartz, R.: Utilizing Spaceborne Radars to Retrieve Dry Snowfall, J. Appl.
671 Meteoro. Climatol., 48, 2564-2580, http://doi.org/10.1175/2009JAMC2193.1, 2009.
672 Kumjian, M. R. and Deierling, W.: Analysis of Thundersnow Storms over Northern Colorado,
673 Weather and Forecasting, 30, 1469-1490, https://doi.org/10.1175/WAF-D-15-0007.1, 2015.
674 Lei, H., Wei, C., Shen, Z., Liang, G., and Li, Y.: Microwave Radiomertric Measurement on
675 Water Vapor and Cloud Liquid Water before Rainfall, Quarterly Journal of Applied
676 Meteorology, 12, 73-79 (in Chinese). 2001.
677 Li, H., Moisseev, D., and von Lerber, A.: How Does Riming Affect Dual-Polarization Radar
678 Observations and Snowflake Shape?, Journal of Geophysical Research Atmospheres, 123,
679 6070–6081, http://doi.org/10.1029/2017JD028186, 2018.
680 Li, J., Zhao, S., and Sun, J.: Analysis of a Record Heavy Snowfall Event in North China,
681 Climatic and Environmental Research, 22, 683-698 (in Chinese). 2017.
682 Li, J., Li, G. e., Pei, Y., Wang, F., Wang, X., and Wen, J.: Analysis on the Phase
683 Transformation of Precipitation During a Strong Cold Wave Happened in Spring,
684 Meteorological Monthly, 35, 87-94 (in Chinese). 2009.
685 Liao, L., Meneghini, R., Tokay, A., and Bliven, L. F.: Retrieval of Snow Properties for Ku-
686 and Ka-Band Dual-Frequency Radar, Journal of Applied Meteorology and Climatology, 55,
687 1845-1858, 2016.
688 Low, T. B. and List, R.: Collision, Coalescence and Breakup of Raindrops. Part I:
689 Experimentally Established Coalescence Efficiencies and Fragment Size Distributions in
690 Breakup, Journal of Atmospheric Sciences, 39, 1591-1606, https://doi.org/10.1175/1520-
691 0469(1982)039<1591:CCABOR>2.0.CO;2, 1982.
692 Ma, X., Dong, X., Bi, K., Wen, D., Chen, Y., Chen, Y., and Mai, R.: The characteristics and
693 evolution of low trough snowfall cloud system in the Haituo mountain， Beijing, Acta
694 Meteorologica Sinica, 79, 428-442 (in Chinese). 2021.
695 Maahn, M. and Kollias, P.: Improved Micro Rain Radar snow measurements using Doppler
696 spectra post-processing, Atmos. Meas. Tech., 5, 2661-2673, http://doi.org/10.5194/amt-5-
697 2661-2012, 2012.
698 Mai, L., Yang, S., Wang, Y., and Li, R.: Impacts of Shape Assumptions on Z–R Relationship
699 and Satellite Remote Sensing Clouds Based on Model Simulations and GPM Observations,
700 Remote Sensing, 15, 1556, http://doi.org/10.3390/rs15061556, 2023.
701 Makino, K., Shiina, T., and Ota, M.: A precipitation classification system using vertical
702 doppler radar based on neural networks, Radio Science, 54, 20-33,
703 http://doi.org/10.1029/2018RS006567, 2019.
704 Matrosov, S. Y.: Modeling Backscatter Properties of Snowfall at Millimeter Wavelengths,
705 Journal of the Atmospheric Sciences, 64, 1727-1736, https://doi.org/10.1175/JAS3904.1, 2007.
706 Matrosov, S. Y., Campbell, C., Kingsmill, D., and Sukovich, E.: Assessing Snowfall Rates
707 from X-Band Radar Reflectivity Measurements, Journal of Atmospheric and Oceanic
708 Technology, 26, 2324-2339, https://doi.org/10.1175/2009JTECHA1238.1, 2009.

https://doi.org/10.5194/egusphere-2026-1706
Preprint. Discussion started: 4 May 2026


McFarquhar, G. M., Finlon, J. A., Stechman, D. M., Wu, W., Jackson, R., and Freer, M.: University of Illinois/Oklahoma optical array probe (OAP) processing software [code], https://doi.org/10.5281/zenodo.1285969., 2018.

Murakami, M.: Inner Structures of Snow Clouds over the Sea of Japan Observed by Instrumented Aircraft: A Review, Journal of the Meteorological Society of Japan. Ser. II, 97, 5-38, 10.2151/jmsj.2019-009, 2019.

Noh, Y.-J., Liu, G., and Seo, E.-K.: Development of a snowfall retrieval algorithm using data at high microwave frequencies, Journal of Geophysical Research, 111, D22216, 2006.

Pei, Y., Wang, F., Zhang, Y., and Wang, L.: Analysis on Doppler Radar Feature of Snowstorm in Hebei in Late Autumn of 2009, Plateau Meteorology, 31, 1110-1118 (in Chinese). 2012.

Peng, X., Kong, Z., Zhang, Z., and Zhao, F.: Study on Discrimination Indicators for Precipitation Types during Winter in Zhejiang Province, Journal of Zhejiang Meteorology, 36, 8-13(in Chinese). 10.16000/j.cnki.zjqx.2015.03.004, 2015.

Peters, G., Fischer, B., Münster, H., Clemens, M., and Wagner, A.: Profiles of Raindrop Size Distributions as Retrieved by Microrain Radars, Journal of Applied Meteorology, 44, 1930-1949, https://doi.org/10.1175/JAM2316.1, 2005.

Reynolds, S. E., Brook, M., and Gourley, M. F.: Thunderstorm Charge Separation, J. Atmos. Sci., 14, 426-436, https://doi.org/10.1175/1520-0469(1957)014<0426:TCS>2.0.CO;2, 1957.

Rosenfeld, D. and Ulbrich, C. W.: Cloud Microphysical Properties, Processes, and Rainfall Estimation Opportunities, Meteorological Monographs, 30, 237-258, https://doi.org/10.1175/0065-9401(2003)030<0237:CMPPAR>2.0.CO;2, 2003.

Saunders, C. P. R., Keith, W., and Mitzeva, R.: The effect of liquid water on thunderstorm charging, Journal of Geophysical Research, 96, 11007-11017, http://doi.org/10.1029/91JD00970, 1991.

Song, C.: Dataset for a snowfall event [dataset], https://doi.org/10.5281/zenodo.19329115, 2026.

Souverijns, N., Gossart, A., Lhermitte, S., Gorodetskaya, I. V., Kneifel, S., Maahn, M., Bliven, F. L., and van Lipzig, N. P. M.: Estimating radar reflectivity - Snowfall rate relationships and their uncertainties over Antarctica by combining disdrometer and radar observations, Atmospheric Research, 196, 211-223, https://doi.org/10.1016/j.atmosres.2017.06.001, 2017.

Szyrmer, W. and Zawadzki, I.: Snow Studies. Part II: Average Relationship between Mass of Snowflakes and Their Terminal Fall Velocity, Journal of the Atmospheric Sciences, 67, 3319-3335, https://doi.org/10.1175/2010JAS3390.1, 2010.

Tao, R., Zhao, K., Huang, H., Wen, L., Zhang, G., Zhou, A., and Chen, H.: Snow Particle Size Distribution From a 2-D Video Disdrometer and Radar Snowfall Estimation in East China, IEEE Transactions on Geoscience and Remote Sensing, 59, 196-207, http://doi.org/10.1109/TGRS.2020.2990920, 2021.

Tokay, A., Hartmann, P., Battaglia, A., Gage, K. S., Clark, W. L., and Williams, C. R.: A Field Study of Reflectivity and Z–R Relations Using Vertically Pointing Radars and Disdrometers, Journal of Atmospheric and Oceanic Technology, 26, 1120-1134, https://doi.org/10.1175/2008JTECHA1163.1, 2009.

Trefalt, S., Martynov, A., Barras, H., Besic, N., Hering, A. M., Lenggenhager, S., Noti, P., Röthlisberger, M., Schemm, S., Germann, U., and Martius, O.: A severe hail storm in complex

https://doi.org/10.5194/egusphere-2026-1706
Preprint. Discussion started: 4 May 2026


752 topography in Switzerland - Observations and processes, Atmospheric Research, 209, 76-94,
753 https://doi.org/10.1016/j.atmosres.2018.03.007, 2018.
754 Wang, H., Lei., H., and Yang, J.: Microphysical Processes of a Stratiform Precipitation Event
755 over Eastern China: Analysis Using Micro Rain Radar data, Advances in Atmospheric
756 Sciences, 34, 1472-1482, http://doi.org/10.1007/s00376-017-7005-6, 2017.
757 Wang, H., Yang, J., Gong, D., Wang, J., Zhang, D., Sun, S., and Chen, S.: Inversion of
758 Precipitation Parameters and Precipitation Type Classification Based on Micro Rain Radar,
759 Chinese Journal of Atmospheric Sciences, 47, 739-755. (in Chinese), 10.3878/j.issn.1006-
760 9895.2201.21210, 2023a.
761 Wang, Y., Kong, R., Cai, M., Zhou, Y., Song, C., Liu, S., Li, Q., Chen, H., and Zhao, C.: High
762 small ice concentration in stratiform clouds over Eastern China based on aircraft observations:
763 Habit properties and potential roles of secondary ice production, Atmospheric Research, 281,
764 106495, https://doi.org/10.1016/j.atmosres.2022.106495, 2023b.
765 Wen, G., Xiao, H., Yang, H., Bi, Y., and Xu, W.: Characteristics of summer and winter
766 precipitation over northern China, Atmospheric Research, 197, 390-406,
767 https://doi.org/10.1016/j.atmosres.2017.07.023, 2017.
768 Wen, J., Wang, G., Zhou, R., Li, R., Zhaxi, S., and Bai, M.: Seasonal Variation in Vertical
769 Structure for Stratiform Rain at Mêdog Site in Southeastern Tibetan Plateau, Remote Sensing,
770 16, 1230, 2024.
771 Wen, L., Zhao, K., Zhang, G., Xue, M., and Chen, X.: Statistical Characteristics of Raindrop
772 Size Distributions Observed in East China during the Asian Summer Monsoon Season using
773 2D-Video Disdrometer and Micro-rain Radar Data, Journal of Geophysical Research
774 Atmospheres, 121, 2265-2282, 2016.
775 Woods, C. P., Stoelinga, M. T., and Locatelli, J. D.: Size Spectra of Snow Particles Measured
776 in Wintertime Precipitation in the Pacific Northwest, Journal of the Atmospheric Sciences, 65,
777 189-205, 2008.
778 Wu, J., Bi, Y., Sun, Q., and Lv, D.: Observation and Analysis of Snowband Structure in a
779 Process of Cyclone Frontal Snowfall in Beijing with Ka-band and X-band Polarized Radars,
780 Chinese Journal of Atmospheric Sciences 45, 931-942, 2021.
781 Xiao, H., Zhang, F., He, Q., Liu, P., and Yang, Z.: Classification of Ice Crystal Habits
782 Observed From Airborne Cloud Particle Imager by Deep Transfer Learning, Earth and Space
783 Science, 6, 1877-1886, http://doi.org/10.1029/2019EA000636, 2019.
784 Xu, A., Qiao, L., Zhan, F., and Niu, X.: Diagnosis of a Cold Wave Weather Event in March
785 2005, Meteorological Monthly, 49-55 (in Chinese). 2006.
786 Xu, H. and Zong, Z.: Analysis on Characteristics of Thermal Vertical Structure Evolution
787 During the Transition of Precipitation Type in Winter, Plateau Meteorology, 33, 1272-1280 (in
788 Chinese). 2014.
789 Yuter, S. E. and Houze, R. A.: Three-Dimensional Kinematic and Microphysical Evolution of
790 Florida Cumulonimbus. Part II: Frequency Distributions of Vertical Velocity, Reflectivity, and
791 Differential Reflectivity, Monthly Weather Review, 123, 1941-1963,
792 https://doi.org/10.1175/1520-0493(1995)123<1941:TDKAME>2.0.CO;2, 1995.
793 Zhang, Z. and Zhou, Y.: Analyses of Composite Observations of Cloud Liquid Waterand
794 Precipitation on the Evolution Features, Meteorological Monthly, 36, 83-89 (in Chinese).
795 2010.

https://doi.org/10.5194/egusphere-2026-1706
Preprint. Discussion started: 4 May 2026


796 Zhao, W., Huang, H., Zhao, K., Lu, Y., Li, A., Pan, X., Chen, H., and Hu, X.: Potential of
797 Fully Connected Neural Networks for Microphysical Retrieval of Ice Hydrometeors From
798 Dual-Polarization Radar Data, Geoscience and Remote Sensing, IEEE Transactions on, 63, 1-
799 16, 2025.
800 Zhou, L., Zhou, Y., Fu, Z., Lü, J., Lu, C., and Xiao, H.: Vertical structures and microphysical
801 mechanisms of winter precipitation over the southwestern mountainous area of China,
802 Atmospheric Research, 303, 107346, https://doi.org/10.1016/j.atmosres.2024.107346, 2024.
803 Zhou , Z. and Guo, X.: A three dimensional modeling study of multi-layer dist ribution and
804 formation processes of electric charge in a severe thunderstorm, Chinese Journal of
805 Atmospheric Sciences, 33, 600-620 (in Chinese). 2009.
806
807